






Blocking an N-terminal acetylation-dependent protein interaction inhibits an E3 ligase

Daniel C Scott^{1,2,10}, Jared T Hammill^{3,9,10}, Jaeki Min³, David Y Rhee⁴ , Michele Connelly³, Vladislav O Sviderskiy¹, Deepak Bhasin³, Yizhe Chen^{3,9} , Su-Sien Ong³, Sergio C Chai³, Asli N Goktug³, Guochang Huang⁵, Julie K Monda¹, Jonathan Low³, Ho Shin Kim^{3,9}, Joao A Paulo⁴ , Joe R Cannon⁴, Anang A Shelat³ , Taosheng Chen³, Ian R Kelsall⁶ , Arno F Alpi⁷, Vishwajeeth Pagala⁸, Xusheng Wang⁸, Junmin Peng^{1,8}, Bhuvanesh Singh⁵, J Wade Harper⁴, Brenda A Schulman^{1,2*} & R Kip Guy^{3,9*} 

N-terminal acetylation is an abundant modification influencing protein functions. Because ~80% of mammalian cytosolic proteins are N-terminally acetylated, this modification is potentially an untapped target for chemical control of their functions. Structural studies have revealed that, like lysine acetylation, N-terminal acetylation converts a positively charged amine into a hydrophobic handle that mediates protein interactions; hence, this modification may be a druggable target. We report the development of chemical probes targeting the N-terminal acetylation-dependent interaction between an E2 conjugating enzyme (UBE2M or UBC12) and DCN1 (DCUN1D1), a subunit of a multiprotein E3 ligase for the ubiquitin-like protein NEDD8. The inhibitors are highly selective with respect to other protein acetyl-amide-binding sites, inhibit NEDD8 ligation *in vitro* and in cells, and suppress anchorage-independent growth of a cell line with DCN1 amplification. Overall, our data demonstrate that N-terminal acetyl-dependent protein interactions are druggable targets and provide insights into targeting multiprotein E2-E3 ligases.

Protein N termini are hotbeds for modifications that influence the interactions and homeostasis of many proteins¹.

A widespread conserved eukaryotic modification is N-terminal acetylation. Approximately 80% of mammalian cytosolic proteins are subject to either co- or post-translational modification by N-terminal acetyltransferases (NATs)^{2,3}. N-terminal acetylation plays essential roles in cell proliferation, apoptosis, chromatin remodeling, protein trafficking, and other fundamental biological processes^{2,4-7}. Mutations in some NAT enzymes have been linked to devastating human diseases^{8,9}. At the molecular level, acetylation transforms the positively charged N terminus into a hydrophobic handle by capping the amino group as an amide containing an additional methyl group³. N-terminal acetylation status can influence protein properties including folding, oligomerization, and intermolecular interactions³. Potentially therapeutically relevant roles of protein interactions regulated by N-terminal acetylation include assembly of an E2-E3 ubiquitin-like protein-ligation complex, nucleosome binding by an epigenetic regulator, cytoskeletal organization, integrity of the anaphase-promoting complex, and E3 ligase-substrate interactions¹⁻¹².

Given the prevalence and importance of N-terminal acetylation, we sought to determine whether chemical disruption of a protein-protein interaction controlled by this modification might be useful for manipulating processes regulated by this modification. To our knowledge, there are no small molecules targeting binding pockets for acetylated N termini. The recent development of small molecules targeting binding pockets for acetylated lysines suggests that inhibiting interactions mediated by acetylated N termini would be possible^{2,13-15}. To address this possibility, we focused on the interaction

between the N-terminally acetylated E2 conjugating (UBE2M, also known as UBC12) and E3 ligase (DCN1, also known as DCUN1D1, DCNLI, and SCCRO) enzymes for the ubiquitin-like protein NEDD8 (Fig. 1a). The molecular role of UBE2M's acetylated N terminus is structurally understood, and the acetyl group contributes approximately two orders of magnitude to the binding energy¹⁰.

The N-terminal acetylation-dependent interaction of UBE2M with DCN1 regulates assembly of a multiprotein complex catalyzing NEDD8 ligation to cullin proteins (Supplementary Results, Supplementary Fig. 1a). This process, termed 'neddylation', controls the activities of the cullins in ubiquitin-ligation cascades. During neddylation, the acetylated N-terminal methionine from UBE2M docks into a pocket in DCN1, which was named on the basis of its loss of function in yeast and worms, causing defective cullin neddylation^{10,16-20}. Within the multiprotein NEDD8 E3 ligase complex, the RING E3 RBX1 (which has multiple functions in neddylation and ubiquitination) binds both the E2 catalytic domain from UBE2M and the cullin substrate. DCN1 stabilizes the catalytic complex by binding the cullin's substrate WHB domain and UBE2M's acetylated N terminus on a flexibly tethered helix^{10,19-21} (Fig. 1a). Mammals express five DCN paralogs with 30-80% sequence identity over their E3 'potentiation of neddylation' (PONY) domains, which combinatorially regulate the neddylation of six homologous cullin proteins via distinct but overlapping expression patterns and cellular locations^{10,16,19,22,23}. Although downstream targets that are regulated by the human DCN1 pathway remain unknown, the *DCN1* gene is amplified along the 3q26.3 region in most squamous cell carcinomas²⁴. *DCN1* amplification negatively correlates with cause-specific survival, and high DCN1 protein levels have been

¹Department of Structural Biology, St. Jude Children's Research Hospital, Memphis, Tennessee, USA. ²Howard Hughes Medical Institute, St. Jude Children's Research Hospital, Memphis, Tennessee, USA. ³Department of Chemical Biology and Therapeutics, St. Jude Children's Research Hospital, Memphis, Tennessee, USA. ⁴Department of Cell Biology, Harvard Medical School, Boston, Massachusetts, USA. ⁵Laboratory of Epithelial Cancer Biology, Memorial Sloan-Kettering Cancer Center, New York, New York, USA. ⁶MRC Protein Phosphorylation and Ubiquitylation Unit, University of Dundee, Dundee, UK. ⁷Department of Molecular Machines and Signaling, Max Planck Institute of Biochemistry, Martinsried, Germany. ⁸St. Jude Proteomics Facility, St. Jude Children's Research Hospital, Memphis, Tennessee, USA. ⁹Present address: Department of Pharmaceutical Sciences, University of Kentucky, Lexington, Kentucky, USA. ¹⁰These authors contributed equally to this work. *e-mail: brenda.schulman@stjude.org or kip.guy@uky.edu

associated with anchorage-independent growth in soft agar, thus suggesting that targeting DCN1 may be of clinical utility^{17,23–25}.

Herein, we report the discovery of potent and selective small-molecule inhibitors of the interaction of *N*-acetyl-UBE2M with DCN1. Overall, the data demonstrate that *N*-terminal acetylation is a druggable target, establish paradigms for selectively inhibiting *N*-terminal acetylation-dependent protein interactions, and provide routes for inhibiting a specific E2–E3 ubiquitin-like protein–ligase complex.

RESULTS

Antagonizing the *N*-acetyl-UBE2M–DCN1 complex

We developed a ligand competition assay on the basis of prior mapping of the motifs mediating interactions between DCN1 (PONY domain alone) and UBE2M (acetylated *N*-terminal peptide)^{10,18,19} (Supplementary Fig. 1b). The time-resolved fluorescence energy transfer (TR-FRET) signal between a biotinylated version of DCN1 (recognized by terbium-linked streptavidin) and a stapled peptide corresponding to *N*-terminally acetylated UBE2M (C-terminally labeled with Alexa Fluor 488) was used to screen a library containing 601,194 unique chemicals at a fixed concentration of 30 μM for each test article (Supplementary Table 1 and Supplementary Fig. 2). The primary screen yielded an average final z' of 0.56, and the fidelity of the assay for selecting true positives, determined by receiver operating characteristic analysis, demonstrated good discriminatory power (area under the curve ~ 0.74) and indicated that a cutoff of $>45\%$ activity would retain $>80\%$ of the true positives (Supplementary Fig. 2). 856 hits (0.15% hit rate) were tested for dose-dependent responses in the TR-FRET assay (Supplementary Data Set 1), thus yielding 182 validated hits with half-maximal inhibitory concentration (IC_{50}) $<15 \mu\text{M}$. Chemical-structure analysis through topology mapping and clustering²⁶ revealed several chemotypes, including multiple scaffolds with promising structure–activity relationships (SARs) (Supplementary Fig. 3a). Scaffolds were prioritized on the basis of dose–response potency, SAR range (ten-fold or more), solubility ($\geq 10 \mu\text{M}$), permeability ($\geq 200 \times 10^{-6} \text{ cm/s}$), and low cytotoxicity toward untransformed BJ fibroblasts. Scaffolds that contained PAINS²⁷ motifs or were noncompliant with Lipinski's rule of five²⁸ were deprioritized.

Three structural clusters sharing a pharmacophore element consisting of an *N*-benzyl (or benzoyl) piperidine could be grouped into a single series of compounds represented by the inhibitor compound NAcM-HIT (1) (Supplementary Figs. 1c and 3b). The unifying feature among the three scaffolds is a piperidine ring that adds 3D character. Resynthesized NAcM-HIT inhibited DCN1 binding to the *N*-terminally acetylated UBE2M peptide (IC_{50} of 7 μM) (Supplementary Fig. 1c). We tested whether NAcM-HIT inhibited the neddylation reaction catalyzed by the larger multi-protein complex containing this E2–E3 subcomplex (Fig. 1a). To isolate the E2–E3-dependent step in NEDD8's E1–E2–E3 cascade (Supplementary Fig. 1a), we used a pulse–chase assay, as previously described^{10,20}. First, the UBE2M~NEDD8 intermediate (in which \sim denotes thioester linkage) is generated in a 'pulse' reaction catalyzed by the NEDD8 E1 in the presence of UBE2M, fluorescent NEDD8, and Mg-ATP. After quenching of this pulse reaction, neddylation is monitored by tracking the 'chase' of fluorescent NEDD8 from UBE2M to the acceptor lysine on a cullin–RBX1 complex in the presence or absence of DCN1 (ref. 10). NAcM-HIT blocked DCN1-dependent cullin neddylation with an IC_{50} of 4 μM in this assay (Fig. 1b and Supplementary Fig. 1c). Importantly, NAcM-HIT did not inhibit the much slower DCN1-independent NEDD8 ligation reaction, which does not depend on acetylation of UBE2M's *N* terminus¹⁰ (Fig. 1b).

To aid in compound optimization and to determine mechanisms by which NAcM-HIT inhibits DCN1–UBE2M interactions and DCN1-dependent neddylation, we sought to obtain structural data.

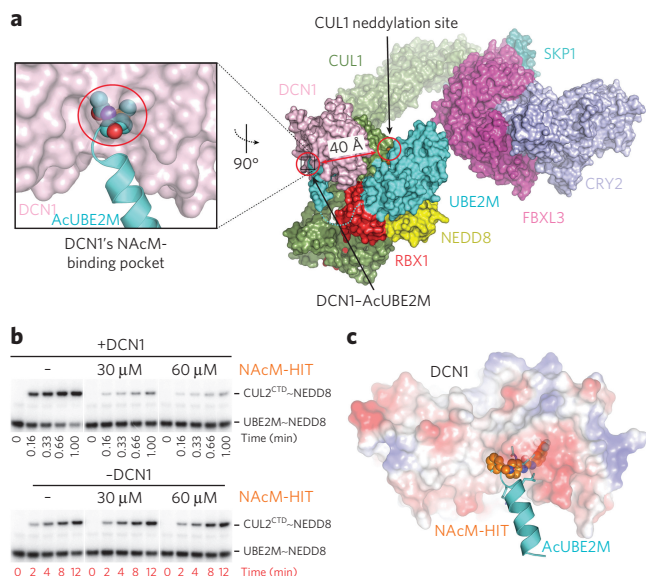


Figure 1 | Discovery of small-molecule inhibitors targeting the interaction of *N*-acetyl-UBE2M with DCN1. (a) Model of a neddylation complex, highlighting DCN1 (pink) interactions with the acetylated *N* terminus of UBE2M (cyan), including structures of CUL1 (green)–RBX1 (red) and SKP1 (pale cyan)–FBXL3 (magenta)–substrate (CRY2, light blue)²⁰. Although it is $\sim 40 \text{ \AA}$ from the CUL1 neddylation site, the interaction between DCN1 and *N*-acetyl-UBE2M (AcUBE2M) accelerates neddylation²⁰. (b) Pulse-chase assays monitoring effects of the indicated concentrations of NAcM-HIT on DCN1-dependent (top, timescale 0–1 min) or DCN1-independent (bottom, timescale 0–12 min) neddylation from AcUBE2M to the CUL2 C-terminal domain. The gel scans are representative of a single experiment that was repeated three independent times. (c) Structure of DCN1 (surface colored on the basis of electrostatic potential) bound to NAcM-HIT (spheres, orange) aligned to DCN1 (omitted for clarity)–AcUBE2M (cyan), demonstrating that NAcM-HIT binds to DCN1's NAcM-binding pocket.

Initial crystal forms were hindered by the small molecule occupying crystal-packing interfaces. To identify crystal forms suitable for structure-based-inhibitor design, we tested 16 different versions of DCN1. Ultimately, a fusion of a mutant T4 lysozyme immediately *N* terminal of DCN1's PONY domain allowed us to obtain crystals with DCN1's *N*-acetylmethionine (NAcM)-binding pocket oriented toward solvent (Supplementary Fig. 4a and Supplementary Table 2). The 2.0- \AA -resolution co-crystal structure with NAcM-HIT demonstrated that the lysozyme fusion did not perturb DCN1's fold (r.m.s. deviations of 1.0 \AA and 1.2 \AA compared with structures of DCN1 bound to acetylated peptide or full-length versions of UBE2M, respectively^{10,20}) (Supplementary Fig. 4b). Importantly, NAcM-HIT occupies the targeted NAcM-binding pocket in DCN1 (Fig. 1c).

Structure-based optimization of NAcM inhibitors

Our screening collection contained >300 compounds related to NAcM-HIT but with varying potency, thus allowing for initial capture of SAR (Supplementary Data Set 2). The screening-set SAR together with structural data for DCN1 binding to NAcM-HIT or *N*-terminally acetylated UBE2M^{10,19,20} revealed five subpockets within DCN1 that could be targeted to improve compound affinity (Fig. 2a). The isoleucine, *N*-acetyl, and leucine subpockets represent areas of the binding pocket occupied by those moieties from UBE2M, and the urea and hinge pockets represent areas populated by those substructures of NAcM-HIT (Fig. 2a). The SAR revealed the following trends: (i) the solvent-exposed isoleucine pocket tolerated a wide range of substituents; (ii) the central piperidine core was critical to activity, and alterations in its size or substitution pattern

decreased potency; (iii) a hydrogen-bond donor in the urea pocket was important, but the urea itself could be replaced with either an amide or a benzothiazole; (iv) the hinge pocket tolerated only a narrow range of substituents, and even minor deviations from the *meta*-substituted six-membered aromatic ring caused substantial decreases in activity.

We used iterative structure-based optimization to select moieties to fill the subpockets, paying particular attention to hydrogen-bonding and electrostatic interactions. We generated more than 300 analogs and tested them in TR-FRET assays, and collected and refined X-ray crystallography data to the point of being able to view $F_o - F_c$ density showing more than 20 of these analogs bound to DCN1. A key observation was that a moderately sized hydrophobic group filling the leucine pocket significantly increased affinity. Overall, iterative examination of the TR-FRET-based dose–response curves, together with electron density maps, indicated four key drivers of potency: (i) the piperidine linker that orients the ends of the molecule into the hydrophobic isoleucine and hinge subpockets, (ii) a hydrogen bond between the urea aryl N-H and the backbone from DCN1's Gln114, which anchors the inhibitor into the binding site, (iii) tight steric packing of the hinge pocket around the substituted phenyl ring, and (iv) hydrophobic interactions of the benzyl substituent within the leucine region. Ultimately, an optimized inhibitor, NAcM-OPT (2), was designed to exploit all four interactions. NAcM-OPT (IC_{50} of 80 nM) showed 100-fold-enhanced potency relative to NAcM-HIT in inhibiting the interaction. The improved inhibition of the isolated E2-E3 interaction translated into a 25-fold-increased potency toward the neddylation reaction carried out by a fully assembled neddylation complex (Fig. 2c and Supplementary Fig. 5).

A 1.4-Å-resolution co-crystal structure showed consolidation of numerous structural elements from DCN1 contributing to the high-affinity interaction with NAcM-OPT (Fig. 2d and Supplementary Fig. 6a–d). First, side chains from two internal aromatic residues, Phe109 and Phe117, are displaced relative to their positions in previous DCN1 structures, thus establishing a substantially deeper hydrophobic pocket for the substituted phenyl ring to access. Second, several hydrophobic residues from DCN1 (Ile86, Phe89, Ala111, Phe117, Phe122, and Phe164) coalesce around the phenyl ring and consequently produce the tightly fitting hinge pocket. Third, the internal rearrangements of DCN1's hinge pocket appear to be necessary to place the urea aryl N-H for hydrogen-bonding with the backbone of Gln114 from DCN1, thus effectively positioning the compound (Supplementary Fig. 6c,d). The four-carbon alkyl linker anchors snugly into the isoleucine pocket through hydrophobic interactions with DCN1 Ala98 and Leu184, and through stacking with the aromatic ring of Tyr181. DCN1's Ile83 and Ile86 contact the benzyl substituent in the leucine subpocket and stabilize the interaction.

These structural principles guided development of additional NAcM probes (Fig. 2b). First, we developed the inactive control molecule NAcM-NEG (3) by mimicking the electrostatic repulsion driven by the positive charge of unacetylated UBE2M's N terminus by replacing the hydrophobic dichlorophenyl ring with a polar pyridine ring (Supplementary Fig. 6e). As predicted, NAcM-NEG had no effect on the interaction between DCN1 and UBE2M, as monitored by TR-FRET, and no effect on neddylation, as monitored by enzyme assays, even at concentrations of 100 μ M (Fig. 2c).

Second, we designed a covalent inhibitor targeting DCN1's Cys115, located within 10 Å of the benzyl substituent (Supplementary Fig. 6f). We used TR-FRET to profile 12 analogs of NAcM-OPT with well-characterized cysteine-reactive electrophilic warheads, including chloroacetamides and acrylamides^{29,30}, installed onto the benzyl ring (Supplementary Table 3). The results revealed that warhead positioning was critical. Introduction of electrophiles onto *ortho* or *meta* positions of NAcM-OPT's benzylic ring pro-

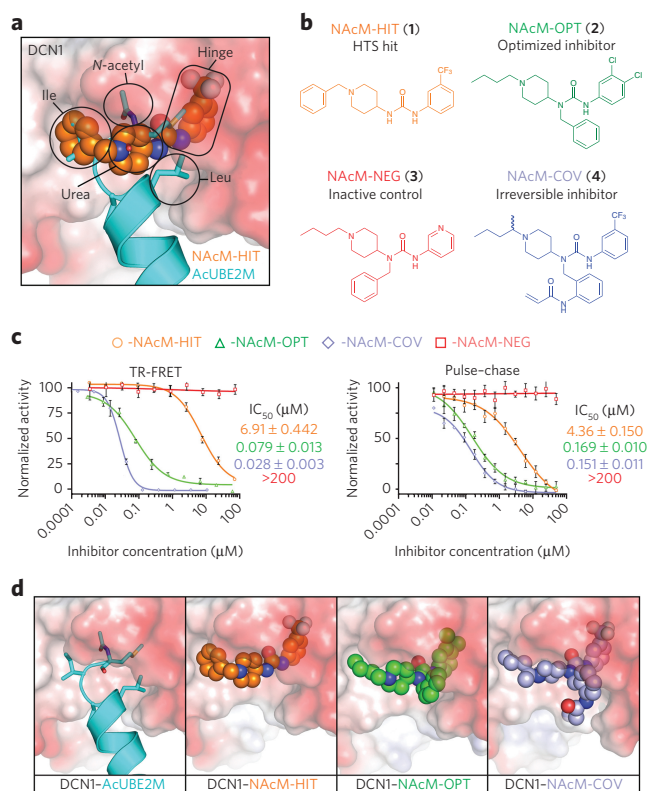


Figure 2 | Structure-based optimization and development of a toolkit of small-molecule probes inhibiting DCN's interaction with UBE2M.

(a) Close-up view of DCN1's UBE2M-binding site with NAcM-HIT (orange) superimposed on N-terminally acetylated UBE2M (AcUBE2M; cyan, PDB 3TDU). The subpockets targeted during structure-based compound optimization are highlighted. (b) Chemical structures, nomenclature, and class of chemical probes targeting DCN's NAcM-binding pocket. NAcM-COV was synthesized and tested as a racemic mixture. Synthetic procedures and characterization data are in **Supplementary Note**. (c) Inhibition of DCN1 binding to an AcUBE2M peptide (TR-FRET assay, left) or DCN1 activation of AcUBE2M-dependent neddylation (pulse-chase enzyme assay, right). TR-FRET values represent averages \pm 1 s.d. of an experiment performed in triplicate and the pulse-chase values are averaged from three independent experiments. (d) Comparison of co-crystal structures of DCN1 (surface electrostatic) bound to AcUBE2M (cyan, PDB 3TDU), NAcM-HIT (orange), NAcM-OPT (green), and NAcM-COV (light blue).

duced potent inhibitors (TR-FRET $IC_{50} \leq 250$ nM; **Supplementary Table 3**; compounds 4–7). Similar compounds including a methylene linker between the aromatic ring and the warhead were also potent inhibitors (**Supplementary Table 3**; compounds 8–11). However, replacing the benzyl substituent with more flexible two- or three-carbon alkyl chains connecting the urea and the electrophile attenuated activity (**Supplementary Table 3**; compounds 12–15). LC/MS analysis of covalent-adduct formation after a 24-h incubation with DCN1 indicated that the *ortho*-N-acrylamide NAcM-COV (4) was most effective (**Supplementary Fig. 7a**). Therefore, we focused on NAcM-COV containing the acrylamide warhead, which affords selectivity for cysteine over other endogenous nucleophiles and is well tolerated in cells^{29,30}. In agreement with irreversible binding, the apparent potency of NAcM-COV increased over time (**Supplementary Fig. 8b**). Although covalent inhibitors do not provide an equilibrium IC_{50} , preincubation of NAcM-COV with DCN1 overnight before the TR-FRET binding assay yielded an apparent IC_{50} of ≤ 40 nM (Fig. 2c and **Supplementary Fig. 8b**).

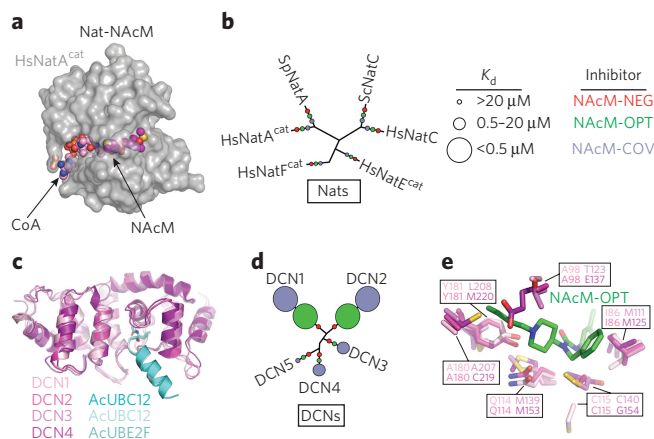


Figure 3 | Optimized NAcM inhibitors display exquisite selectivity for N-acetyl pockets of DCN1 and DCN2. (a) Structure of complex containing NAcM peptide (purple), N-terminal acetyltransferase (hNaa50/NatA (gray), and CoA (pink) (PDB 4X5K). (b) Effects of NAcM-NEG (red), NAcM-OPT (green), and NAcM-COV (light blue) on human (Hs), *Saccharomyces cerevisiae* (Sc), or *Schizosaccharomyces pombe* (Sp) Nat enzymes. K_d values inferred from enzymatic assays (Supplementary Fig. 10) are plotted on a similarity-based dendrogram. (c) Structural superimposition of DCN family members: DCN1 (100% identity, 0 r.m.s. deviation, pink)–N-acetyl-UBE2M (AcUBE2M; cyan, PDB 3TDU), DCN2 (82% identity, 0.46 r.m.s. deviation, magenta)–AcUBE2M (pale cyan, PDB 4GAO), DCN3 (36% identity, 1.35 r.m.s. deviation, violet)–AcUBE2F (teal, PDB 4GBA), and DCN4 (34% identity, 1.57 r.m.s. deviation, purple). (d) Effects of probes on DCN1 neddylation activity. K_d values inferred from pulse–chase assays (Supplementary Fig. 11) plotted as in b. (e) Subtle variations in the targeted binding pocket determine NAcM selectivity profiles. Coloring as in c, with residues potentially contributing to selectivity surrounding NAcM-OPT shown in stick representation.

In our enzymatic assay, performing the preincubation overnight yielded an apparent IC_{50} of 150 nM for blocking the neddylation reaction (Fig. 2c). The importance of the covalent warhead was confirmed with a matched control (NAcM-COVCTRL, 16) with a propionamide substitution incapable of covalent linkage to Cys115 replacing the electrophile (Supplementary Fig. 8a). Comparison of the properties of NAcM-COV and NAcM-COVCTRL revealed that the noncovalent inhibitor retained some activity, whereas the electrophile increased potency by >30-fold in the TR-FRET assay and 2.5-fold in the neddylation experiment (Supplementary Fig. 8b–e). Indeed, covalent linkage to the targeted Cys115 was observed in an X-ray co-structure of NAcM-COV bound to DCN1 (Fig. 2d and Supplementary Fig. 6f) and in MS analysis of DCN1 immunoprecipitates from NAcM-COV-treated cells (Supplementary Fig. 8f,g). Thus, formation of the covalent linkage between NAcM-COV and Cys115 is a critical driver of biochemical potency.

Selectivity for N-acetylmethionine-driven interactions

Because acetyl-dependent protein interactions are prevalent in cells, we broadly examined selectivity by testing whether our compounds inhibited five classes of such interactions. First, we examined interactions by using acetylated lysines as drivers of binding, including more than 50 histone acetylases, bromodomains, and histone deacetylases^{2,13} (Supplementary Fig. 9a). Screening at a fixed concentration of 10 μ M and interrogating putative hits with dose–response studies to 100 μ M revealed that our inhibitors did not significantly affect any of these interactions (Supplementary Fig. 9b and Supplementary Data Sets 3–5). Our results indicated a selectivity of >100-fold against tested acetyl-lysine-binding sites.

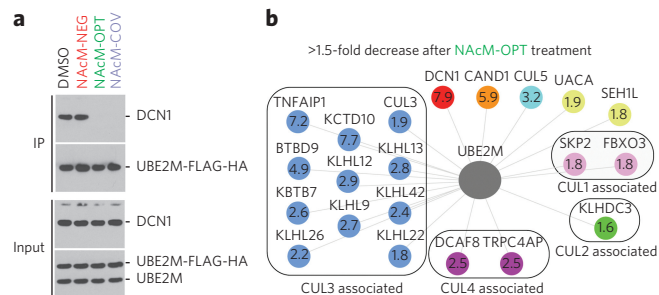


Figure 4 | NAcM inhibitors are on target and disrupt the N-acetyl-UBE2M interaction network. (a) NAcM-OPT and NAcM-COV, but not NAcM-NEG, disrupt coimmunoprecipitation (IP) of DCN1 with N-acetyl-UBE2M. Experiments were performed with 293T cells expressing UBE2M with a C-terminal FLAG-HA tag at near-endogenous levels. Immunoblots of input and eluates from anti-FLAG immunoprecipitations were probed with the indicated antibodies (full gels shown in Supplementary Fig. 14). (b) N-acetyl-UBE2M interactions decreased by >1.5-fold with $P < 0.05$ (calculated using the moderated t statistic (two-sided) with Benjamini–Hochberg false discovery rate adjustment; $n = 3$ independent experiments) by NAcM-OPT (DCN1, red; CAND1, orange) or by association with a particular CRL (CUL1, pink; CUL2, green; CUL3, blue; CUL4A, purple; CUL5, cyan) (Supplementary Data Set 6). The fold decrease in binding is indicated for each protein.

To further interrogate selectivity, we tested activity toward NAT enzymes, which catalyze acetyl transfer from acetyl-CoA to cognate protein N-terminal sequences. UBE2M's methionine-isoleucine N terminus conforms to a substrate of NatC. Even at 25 μ M, our NAcM compounds did not inhibit recombinant trimeric human and yeast NatC enzymes or NatA, NatE, or NatF from various organisms^{10,31–33} (Fig. 3a,b and Supplementary Fig. 10).

Finally, to test for selectivity among the most homologous systems, we examined activity against the five human DCN family members, which have highly similar PONY domains (Fig. 3c) and share overlapping *in vitro* activities of stimulating N-terminally acetylated UBE2M during cullin neddylation^{19,22}. Using our enzymatic assay, examining neddylation in the presence of NAcM-OPT or NAcM-COV at 10 μ M (>50-fold above the IC_{50} with DCN1), NAcM-OPT inhibited only DCN2, whose PONY domain is 82% identical to that of DCN1 (100% identical in the NAcM-binding pocket). NAcM-OPT showed no activity toward DCN3, DCN4, or DCN5, despite high structural similarity (Fig. 3c–e and Supplementary Fig. 11). Side chain differences explained the selectivity of NAcM-OPT (Fig. 3e).

The partial activity of extremely high concentrations (50 μ M) of NAcM-COV toward DCN3 and DCN4 was rationalized by the conservation of the targeted cysteine in DCN3 but was unexpected for DCN4, which has a glycine in this location (Fig. 3d and Supplementary Figs. 7b,c and 11). A 1.55-Å-resolution crystal structure of the DCN4 PONY domain bound to its partner domain from CUL1 revealed Cys219 on the neighboring side of the pocket as having the potential for reactivity with NAcM-COV (Supplementary Table 2 and Supplementary Fig. 7b–d). Notably, the DCN5 sequence lacks cysteines corresponding to Cys115 in DCN1 or Cys219 in DCN4, thus potentially explaining the lack of inhibition by NAcM-COV. We confirmed that the correlation between inhibition by NAcM-COV and the presence of a cysteine in the UBE2M-binding pocket involves covalent modification, by performing TOF-based mass spectrometry after incubating 30 μ M of the PONY domain from each DCN family member overnight with 60 μ M NAcM-COV (Supplementary Fig. 7a,e–h). The predominant species of DCN1, DCN2, and DCN3 corresponded to adducts with NAcM-COV. Both modified and unmodified forms of DCN4

were detected, with no evidence of covalent linkage to DCN5. Replacement of Cys115 in DCN1 by either alanine or glycine residues prevented covalent-adduct formation with NAcM-COV, thus confirming the essential role of Cys115.

Retrospective inspection of previous DCN1 structures indicated that Cys115's side chain is located between *N*-acetyl-Met1 and Leu4 from acetylated UBE2M^{10,20} (Supplementary Fig. 7k). Furthermore, DCN1's massive stimulation of cullin neddylation was essentially eliminated after mutation of Cys115 to alanine, glycine, isoleucine, leucine, threonine, or valine (Supplementary Fig. 7l,m). Thus, although the capacity for the binding pocket to undergo structural rearrangement may be exploited for developing small molecules (Supplementary Fig. 6b–d), the structural requirement of Cys115 for catalytic activity provides a natural constraint that may prove useful in future covalent-inhibitor development.

Together, our results indicated that our toolkit for probing DCN1 interactions with *N*-terminally acetylated UBE2M includes: a reversible inhibitor (NAcM-OPT), an irreversible inhibitor (NAcM-COV), and a structurally matched but inactive control compound (NAcM-NEG; Fig. 2). These compounds are straightforward to synthesize at high yield and purity (Supplementary Note; compounds 17–23), and are highly specific for DCN1 and DCN2, even across the highly structurally and functionally conserved DCN family (Fig. 3). Thus, it is possible to develop small-molecule inhibitors selectively targeting an extraordinarily prevalent protein interaction motif.

NAcMs inhibit DCN1 binding to UBE2M in cells

We tested whether our small molecules inhibit DCN1-UBE2M interactions in cells by using lentivirally expressed UBE2M with a C-terminal FLAG-hemagglutinin (HA) tag at near-endogenous levels in 293T cells (Fig. 4a). C-terminal tagging of UBE2M in 293T cells allowed for its essentially complete *N*-terminal acetylation, and affinity-purified UBE2M binds endogenous DCN1 (refs. 10,34). Accordingly, the UBE2M-DCN1 interaction was observed after affinity purification from cells treated for 24 h with DMSO or the inactive control compound NAcM-NEG (Fig. 4a). However, treatment with the reversible (NAcM-OPT) or irreversible (NAcM-COV) inhibitors blocked coprecipitation of DCN1 with UBE2M (Fig. 4a,b and Supplementary Data Set 6). Therefore, the inhibitors that disrupt interaction of UBE2M and DCN1 in reconstituted systems also disrupt complex formation in cells. Thus, the formation of large cellular signaling complexes can be inhibited by disruption of binding of an *N*-acetylated *N* terminus.

Having shown that inhibitors disrupted DCN1 binding to UBE2M, we examined effects on coassociation with other proteins by AP-MS with a quantitative tandem mass tagging (TMT)-based proteomic method³⁴. Cells were treated with either negative controls (DMSO or NAcM-NEG) or active compounds (NAcM-OPT or NAcM-COV), affinity-purified complexes were processed for decaplex TMT, and summed intensities for reporter ions were used to quantify components present within the complexes. Importantly, the interaction most affected by NAcM-OPT was UBE2M binding to DCN1, which was decreased eight-fold relative to controls (Fig. 4b and Supplementary Data Set 6). The majority of other proteins whose interactions with UBE2M were substantially decreased were also part of the cullin-RING ligase (CRL) network, including 1.9- and 3.2-fold decrease of two cullins (CUL3 and CUL5, respectively), and several CRL-substrate receptors. The 7.7-fold to 1.8-fold decrease in UBE2M association with a cohort of BTB proteins that serve as CUL3-substrate receptors was particularly striking (Fig. 4b) and suggested that, in this cell line, inhibition of UBE2M binding to DCN1 might especially affect CUL3. A drastic decrease in DCN1 binding to cullins was further implicated by the 5.9-fold decrease in association of CAND1, a protein previously shown to associate with DCN1 in a cullin-dependent manner^{18,22}. CAND1 marks inactive cullins that are neither neddylated nor bound to substrate receptors,

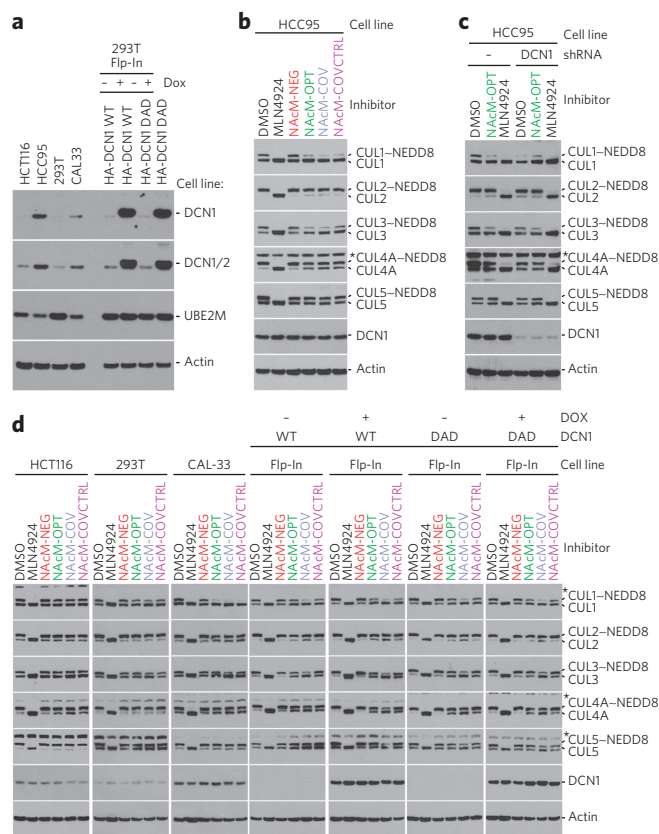


Figure 5 | NAcM inhibitors decrease CUL neddylation in cells and mimic effects of shRNA knockdown of DCN1. (a) HCC95 and CAL-33 have high levels of DCN1, as demonstrated by immunoblotting of total cell extracts of the indicated cell lines (full gels shown in Supplementary Fig. 15a). (b) Effects of NAcM-NEG, NAcM-OPT, NAcM-COV, and NAcM-COVCTRL on cullin neddylation in HCC95 cells treated with DMSO, MLN4924 (single dose, 1 μ M), or the indicated compounds (10 μ M, dosed at 0 and 24 h). Cells were harvested at 48 h, processed for immunoblotting, and probed with the indicated antibodies (full gels shown in Supplementary Fig. 15b). (c) NAcM-OPT mimics shRNA knockdown of DCN1. Immunoblot of total cell extracts from HCC95, or a line stably expressing a DCN1 shRNA, treated and processed as in b (full gels shown in Supplementary Fig. 15c). (d) Probe effects vary among cell lines. Immunoblot of total cell extracts from the indicated cell lines, treated and processed as in b. WT, wild type; DAD, DAD mutant. For all blots, asterisk indicates nonspecific bands in CUL1, CUL4A, and CUL5 immunoblots (full gels shown in Supplementary Fig. 15d–h).

thus raising the possibility that steady-state UBE2M recruitment to CAND1-bound cullins may be DCN1 dependent and perhaps indicating a mechanism for the rapid neddylation of cullins after CAND1 displacement. We did not observe any significant changes in the levels of acetylated UBE2M or any other acetylated peptides detected by our proteomics experiments (Supplementary Fig. 12 and Supplementary Data Set 7).

NAcMs inhibit DCN1-dependent cellular neddylation

In lower eukaryotes that express only a single Dcn1 family member, elimination of Dcn1 or Ubc12 *N*-terminal acetylation leads to a 90% or 50% decrease, respectively, in the steady-state level of neddylated cullins^{10,16,21}; however, in many mammalian cell lines, DCN1 knockdown or knockout has relatively subtle effects on steady-state levels of cullin neddylation^{17,22,35,36}. One possibility is that the other DCN family members, or other regulators, may compensate for loss of DCN1 (refs. 19,22,37,38). Given the greater effects of deleting the

single yeast DCN1 (ref. 16), and prior findings that high-level expression of exogenous human DCN1 modulates cullin neddylation and anchorage-independent growth of human cells cultured on soft agar²⁴, we sought to identify a cell line with high levels of endogenous DCN1 for testing the effects of our inhibitors. Immunoblotting in various human cell lines revealed elevated levels of DCN1 in non-small-cell lung and tongue carcinoma cell lines HCC95 and CAL-33, in agreement with amplification of the *DCUN1D1* gene in most human squamous cell carcinomas (Fig. 5a).

Treatment of HCC95, the cell line expressing the highest levels of DCN1, with NAcM-OPT or NAcM-COV decreased the levels of neddylation detected by immunoblotting to an extent comparable to that observed after knockdown of DCN1 through short hairpin RNA (shRNA) expression (Fig. 5b,c). Combining DCN1 knockdown and treatment with NAcM-OPT resulted in similar decreases in cullin neddylation to those observed after either treatment alone, in agreement with the effects of NAcM-OPT depending on increased levels of DCN1 (Fig. 5b,c). As observed previously for other cell lines^{17,22,35,36}, inhibition of DCN1 activity did not affect all cullins equally. In HCC95 cells, inhibition of DCN1 activity either with NAcM compounds or shRNA primarily affected the steady-state levels of neddylation of CUL1 and CUL3 and had lesser effects on CUL4A. Importantly, the inactive NAcM-NEG had no effect on cullin neddylation status. In concordance with our *in vitro* studies, NAcM-COV exhibited the most potent inhibition of cellular neddylation, whereas NAcM-COVCTRL exhibited relatively decreased potency, thus supporting our hypothesis that covalent linkage with Cys115 drives increased potency of NAcM-COV. Together, these results further support that the suite of NAcM compounds are on target in cells.

To determine whether sensitivity to the inhibitors correlated with DCN1 expression levels, we examined the effects of NAcM compounds in multiple cell lines (Fig. 5a), two with DCN1 amplification (HCC95 and CAL-33), two that have not been reported to have amplification of the *DCN1* gene (HCT116 and 293T), and Flp-IN 293T cell lines bearing doxycycline-inducible transgenes expressing either wild-type DCN1 or a cullin-binding DAD-patch mutant²¹ defective in cullin binding (Fig. 5d). The effects of the NAcMs on steady-state levels of cullin neddylation ranged from subtle effects on levels of neddylation of CUL3 and CUL4A in HCT116 and CUL1 and CUL3 in the parental 293T line to striking decreases in neddylation of CUL1 and CUL3 in CAL-33 and HCC95. Levels of neddylation of CUL2 and CUL5 were not obviously affected in any experiment. These differences suggested that DCN1 levels did correlate to some extent with sensitivity to the NAcMs but also that the DCN1 dependency of a particular cullin family member was cell-type specific. In support of this possibility, induction of WT DCN1 in Flp-IN 293T cells, but not the cullin-binding-defective DAD mutant, mildly sensitized the levels of neddylation of CUL4A to our inhibitors (Fig. 5d).

The effects of inhibiting DCN1-UBE2M interactions markedly differed from those resulting from treatment of cells with the inhibitor of the NEDD8 E1 enzyme MLN4924, which blocks upstream reactions, prevents formation of the UBE2M~NEDD8 intermediate³⁹, and eliminates all observable neddylation in cells (Fig. 5b-d). DCN1 inhibitors and MLN4924 showed the most pronounced cellular effects at concentrations above their respective biochemical IC₉₅ (MLN4924, biochemical IC₅₀ = 5 nM; cell-based activity penetrant at 0.3–1 μM (ref. 39); NAcM, biochemical IC₅₀ = 150–170 nM and in cell based studies, IC₅₀ = 10 μM). Thus, our NAcM inhibitors of DCN1-UBE2M interactions disrupt the function of the targeted multiprotein neddylation-catalyzing complex in cells.

Given the sensitivity of HCC95 cells to DCN1 inhibition, we sought to characterize cellular phenotypes induced by treatment with the suite of NAcM compounds. Although some roles of neddylation in nondegradative ubiquitination are emerging, neddylation is largely recognized for activating ubiquitin-dependent proteasomal degradation. Indeed, total blockade of neddylation by treatment

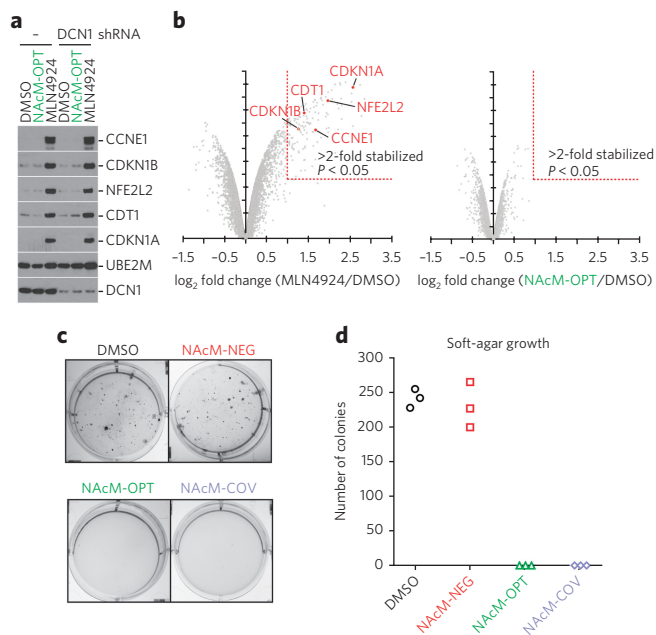


Figure 6 | In a DCN1-amplified cell line, NAcM-OPT inhibits neddylation and prevents anchorage-independent growth without affecting protein homeostasis. (a) Neither NAcM-OPT treatment nor DCN1 shRNA

stabilizes cullin-RING ligase substrates in HCC95 cells. Cells treated and processed as in Figure 5c, with antibodies to the indicated proteins (full gels shown in Supplementary Fig. 16). (b) NAcM-OPT does not globally change protein homeostasis in HCC95 cells. TMT quantification of the total proteome after treatment with DMSO, MLN4924 (left, 1 μM), or NAcM-OPT (right, 10 μM) for 24 h. MLN4924 causes more than two-fold stabilization of 136 proteins ($P < 0.05$, calculated by ANOVA in the LIMMA program.), whereas NAcM-OPT treatment does not stabilize any protein (Supplementary Data Set 8). Substrates examined in a are highlighted in red. (c) NAcM-OPT and NAcM-COV treatment blocks growth of HCC95 cells in soft agar. Representative images showing anchorage-independent growth of HCC95 cells treated with NAcM-OPT (10 μM), NAcM-COV (10 μM), or NAcM-NEG (10 μM). (d) Quantification of results from c.

with MLN4924 decreases total cellular ubiquitination by 10–20%, thereby leading to the stabilization of hundreds of CRL substrates³⁹. Such a role has not been reported for DCN family members. We compared levels of several well-recognized proteasomal targets of cullin-RING ligases after E1 or DCN1 inhibition by immunoblotting. Although control experiments with MLN4924 caused high-level accumulation of CRL substrates, there were no obvious effects on the levels of these substrates after either NAcM inhibition of DCN1 or its knockdown by shRNA (Fig. 6a). Likewise, in an unbiased proteome-wide search, inhibition of DCN1-dependent neddylation starkly contrasted with MLN4924, in that we observed no obviously increasing levels of any proteins measured by TMT-based mass spectrometry (Fig. 6b and Supplementary Data Set 8).

NAcM effects on DCN1-amplified cells

Human DCN1 was originally discovered because of its overexpression in tumor cells, in which amplification confers anchorage-independent growth²⁴. Therefore, we examined the effects of our DCN1/2-specific NAcM probes on the growth of HCC95 cells in 3D culture. Indeed, in the presence of active NAcMs at doses not growth inhibitory toward monolayer cultures (Supplementary Fig. 13), colony formation in soft agar was completely eliminated, whereas treatment with the inactive control had no effect on colony formation (Fig. 6c,d). Thus, inhibiting cell proliferation in soft agar correlates with the functional blockade of DCN1 activity.

DISCUSSION

We showed that selective small-molecule probes can be developed that competitively inhibit protein interactions mediated by N-terminal acetylation. Both the reversible (NAcM-OPT) and irreversible (NAcM-COV) inhibitors were highly specific for blocking the targeted N-terminal acetylation-dependent interaction of UBE2M with DCN1.

Potency was achieved by both populating the pockets normally occupied by the N-terminal methionine side chain of UBE2M and engaging adjacent sites. Unexpected structural rearrangement of residues buried within the targeted pocket enabled our inhibitors to penetrate deeper into a remodeled groove that normally accommodates UBE2M's methionine side chain. Because this deeper groove was not observed in six prior structures of DCN family members in complex with N-terminally acetylated NEDD8 E2s^{10,19,20}, our data underscore the value of empirical screening to harness cryptic protein conformations.

We fortuitously discovered that a cysteine in DCN1's binding pocket is structurally crucial for binding N-terminally acetylated UBE2M. Although our intent was to validate targeting and increase potency, we note that covalent capture of structurally important cysteines has been proposed as an approach to drug targeting⁴⁰. We anticipate that covalent targeting of nonmutable cysteines might also prove useful in mitigating potential resistance mutations.

The specific proteins targeted by inhibiting this N-terminal acetylation-dependent interaction are subunits of an ubiquitin-like protein ligase-conjugating enzyme complex. Despite great interest in targeting ubiquitin and ubiquitin-like protein cascades, discovery of such inhibitors has been hindered by the high homology of E2 and E3 catalytic domains. We demonstrate that exploiting nonhomologous auxiliary E2-E3 interactions within such ligation complexes enables the development of specific molecules that effectively inhibit ligase activity.

The effects of inhibiting this specific NEDD8 E2-E3 interaction are substantially different from those of MLN4924, which obliterates all neddylation by inhibiting the E1 enzyme initiating the NEDD8 cascade. Whereas blocking binding to DCN1 clearly perturbs the UBE2M interactome, there are minimal effects on protein turnover. Perhaps the relatively lower level of neddylation seen with DCN1 inhibition in HCC95 and CAL-33 cells—particularly for CUL1 and CUL3—is sufficient to sustain the CRL network and ubiquitination activity required for CRL-substrate degradation^{37,38}. It remains unknown when cellular neddylation of a particular cullin would involve DCN1 activity²².

Alternatively, DCN1 may specifically associate with a subset of CRLs that catalyze nondegradative ubiquitination. In this regard, it is intriguing that the NAcM inhibitors most strongly impaired neddylation of CUL3, as well as UBE2M interactions with CUL3-associated substrate receptors (Figs. 4 and 5). Notably, proteasome-independent functions of neddylation are beginning to emerge from studies of CUL3 (ref. 41). Challenges in finding nondegradative CRL targets may explain why specific downstream targets of DCN1-dependent cullin neddylation remain unknown. Our finding that inhibition of the DCN1-UBE2M interaction both decreases neddylation and anchorage-independent growth of HCC95 cells with *DCUN1D1* gene amplification highlights the importance of identifying such substrates. In the long term, developing DCN1 inhibitors may prove clinically relevant for treatment of cancers with amplification of the *DCUN1D1* gene, in settings requiring more nuanced regulation of neddylation than that afforded by MLN4924 (pevonedistat) or using combination treatment with MLN4924 as an orthogonal means to inhibit the NEDD8 pathway.

Over the past 20 years, there has been widespread interest in discovering inhibitors of protein-protein interactions through targeting 'hotspots' with small molecules mimicking the clusters of side chains that drive the protein interactions, and several potential

drugs have entered clinical trials. Our development of potent selective inhibitors blocking UBE2M interactions with DCN1, without apparently influencing the N-terminal acetylation status, provides what is, to our knowledge, the first demonstration that these interactions are druggable. Notably, our NAcM inhibitors contrast with Nat enzyme inhibitors, which globally affect protein N-terminal acetylation^{31,32,42}. Although specific interactions involving acetylated protein N termini are only beginning to emerge, some potentially therapeutically relevant targets include ubiquitin E3 ligases, cytoskeletal assemblies, epigenetic regulators, and protein trafficking and quality-control pathways^{1-7,11,12,43,44}. Distinct hydrophobic N termini may also prove to be useful targets for novel therapeutics against devastating pathogens, given that formylmethionine at the N termini of bacterial proteins plays crucial roles in host-pathogen interactions⁴⁵, and some proteins exported from malaria parasites into erythrocytes during infections undergo processing and post-translational N-terminal acetylation⁴⁶. We predict that these or other pathways mediated by acetylation of protein N termini or other nonhistone sites may also be targeted selectively.

Received 21 September 2016; accepted 7 April 2017;
published online 5 June 2017

METHODS

Methods, including statements of data availability and any associated accession codes and references, are available in the [online version of the paper](#).

References

- Varland, S., Osberg, C. & Arnesen, T. N-terminal modifications of cellular proteins: the enzymes involved, their substrate specificities and biological effects. *Proteomics* **15**, 2385–2401 (2015).
- Drazic, A., Myklebust, L.M., Ree, R. & Arnesen, T. The world of protein acetylation. *Biochim. Biophys. Acta* **1864**, 1372–1401 (2016).
- Aksnes, H., Drazic, A., Marie, M. & Arnesen, T. First things first: vital protein marks by N-terminal acetyltransferases. *Trends Biochem. Sci.* **41**, 746–760 (2016).
- Hwang, C.S., Shemorry, A. & Varshavsky, A. N-terminal acetylation of cellular proteins creates specific degradation signals. *Science* **327**, 973–977 (2010).
- van Welsem, T. *et al.* Synthetic lethal screens identify gene silencing processes in yeast and implicate the acetylated amino terminus of Sir3 in recognition of the nucleosome core. *Mol. Cell. Biol.* **28**, 3861–3872 (2008).
- Yi, C.H. *et al.* Metabolic regulation of protein N-alpha-acetylation by Bcl-xL promotes cell survival. *Cell* **146**, 607–620 (2011).
- Forte, G.M., Pool, M.R. & Stirling, C.J. N-terminal acetylation inhibits protein targeting to the endoplasmic reticulum. *PLoS Biol.* **9**, e1001073 (2011).
- Esmailpour, T. *et al.* A splice donor mutation in NAA10 results in the dysregulation of the retinoic acid signalling pathway and causes Lenz microphthalmia syndrome. *J. Med. Genet.* **51**, 185–196 (2014).
- Rope, A.F. *et al.* Using VAAST to identify an X-linked disorder resulting in lethality in male infants due to N-terminal acetyltransferase deficiency. *Am. J. Hum. Genet.* **89**, 28–43 (2011).
- Scott, D.C., Monda, J.K., Bennett, E.J., Harper, J.W. & Schulman, B.A. N-terminal acetylation acts as an avidity enhancer within an interconnected multiprotein complex. *Science* **334**, 674–678 (2011).
- Zhang, Z., Kulkarni, K., Hanrahan, S.J., Thompson, A.J. & Barford, D. The APC/C subunit Cdc16/Cut9 is a contiguous tetratricopeptide repeat superhelix with a homo-dimer interface similar to Cdc27. *EMBO J.* **29**, 3733–3744 (2010).
- Nguyen, T.V. *et al.* Glutamine triggers acetylation-dependent degradation of glutamine synthetase via the thalidomide receptor cereblon. *Mol. Cell* **61**, 809–820 (2016).
- Marmorstein, R. & Zhou, M.M. Writers and readers of histone acetylation: structure, mechanism, and inhibition. *Cold Spring Harb. Perspect. Biol.* **6**, a018762 (2014).
- Filippakopoulos, P. *et al.* Selective inhibition of BET bromodomains. *Nature* **468**, 1067–1073 (2010).
- Nicodeme, E. *et al.* Suppression of inflammation by a synthetic histone mimic. *Nature* **468**, 1119–1123 (2010).
- Kurz, T. *et al.* The conserved protein DCN-1/Dcn1p is required for cullin neddylation in *C. elegans* and *S. cerevisiae*. *Nature* **435**, 1257–1261 (2005).
- Kim, A.Y. *et al.* SCCRO (DCUN1D1) is an essential component of the E3 complex for neddylation. *J. Biol. Chem.* **283**, 33211–33220 (2008).

18. Scott, D.C. *et al.* A dual E3 mechanism for Rub1 ligation to Cdc53. *Mol. Cell* **39**, 784–796 (2010).
19. Monda, J.K. *et al.* Structural conservation of distinctive N-terminal acetylation-dependent interactions across a family of mammalian NEDD8 ligation enzymes. *Structure* **21**, 42–53 (2013).
20. Scott, D.C. *et al.* Structure of a RING E3 trapped in action reveals ligation mechanism for the ubiquitin-like protein NEDD8. *Cell* **157**, 1671–1684 (2014).
21. Kurz, T. *et al.* Dcn1 functions as a scaffold-type E3 ligase for cullin neddylation. *Mol. Cell* **29**, 23–35 (2008).
22. Keuss, M.J. *et al.* Characterization of the mammalian family of DCN-type NEDD8 E3 ligases. *J. Cell Sci.* **129**, 1441–1454 (2016).
23. Fu, W. *et al.* Squamous cell carcinoma-related oncogene (SCCRO) family members regulate cell growth and proliferation through their cooperative and antagonistic effects on cullin neddylation. *J. Biol. Chem.* **291**, 6200–6217 (2016).
24. Sarkaria, I. *et al.* Squamous cell carcinoma related oncogene/DCUN1D1 is highly conserved and activated by amplification in squamous cell carcinomas. *Cancer Res.* **66**, 9437–9444 (2006).
25. Sarkaria, I.S. *et al.* SCCRO expression correlates with invasive progression in bronchioloalveolar carcinoma. *Ann. Thorac. Surg.* **78**, 1734–1741 (2004).
26. Shelat, A.A. & Guy, R.K. Scaffold composition and biological relevance of screening libraries. *Nat. Chem. Biol.* **3**, 442–446 (2007).
27. Baell, J.B. & Holloway, G.A. New substructure filters for removal of pan assay interference compounds (PAINS) from screening libraries and for their exclusion in bioassays. *J. Med. Chem.* **53**, 2719–2740 (2010).
28. Lipinski, C.A., Lombardo, F., Dominy, B.W. & Feeney, P.J. Experimental and computational approaches to estimate solubility and permeability in drug discovery and development settings. *Adv. Drug Deliv. Rev.* **46**, 3–26 (2001).
29. Finlay, M.R. *et al.* Discovery of a potent and selective EGFR inhibitor (AZD9291) of both sensitizing and T790M resistance mutations that spares the wild type form of the receptor. *J. Med. Chem.* **57**, 8249–8267 (2014).
30. Singh, J., Petter, R.C., Baillie, T.A. & Whitty, A. The resurgence of covalent drugs. *Nat. Rev. Drug Discov.* **10**, 307–317 (2011).
31. Liszczak, G. *et al.* Molecular basis for N-terminal acetylation by the heterodimeric NatA complex. *Nat. Struct. Mol. Biol.* **20**, 1098–1105 (2013).
32. Støve, S.I. *et al.* Crystal structure of the golgi-associated human N α -acetyltransferase 60 reveals the molecular determinants for substrate-specific acetylation. *Structure* **24**, 1044–1056 (2016).
33. Van Damme, P. *et al.* Proteome-derived peptide libraries allow detailed analysis of the substrate specificities of N α -acetyltransferases and point to hNaa10p as the post-translational actin N α -acetyltransferase. *Mol. Cell Proteomics* **10**, M110.004580 (2011).
34. Huttlin, E.L. *et al.* The BioPlex Network: a systematic exploration of the human interactome. *Cell* **162**, 425–440 (2015).
35. Huang, G., Kaufman, A.J., Ramanathan, Y. & Singh, B. SCCRO (DCUN1D1) promotes nuclear translocation and assembly of the neddylation E3 complex. *J. Biol. Chem.* **286**, 10297–10304 (2011).
36. Meyer-Schaller, N. *et al.* The human Dcn1-like protein DCN1L promotes Cul3 neddylation at membranes. *Proc. Natl. Acad. Sci. USA* **106**, 12365–12370 (2009).
37. Lydeard, J.R., Schulman, B.A. & Harper, J.W. Building and remodelling Cullin-RING E3 ubiquitin ligases. *EMBO Rep.* **14**, 1050–1061 (2013).
38. Deshaies, R.J., Emberley, E.D. & Saha, A. Control of cullin-ring ubiquitin ligase activity by nedd8. *Subcell. Biochem.* **54**, 41–56 (2010).
39. Soucy, T.A. *et al.* An inhibitor of NEDD8-activating enzyme as a new approach to treat cancer. *Nature* **458**, 732–736 (2009).
40. Serafimova, I.M. *et al.* Reversible targeting of noncatalytic cysteines with chemically tuned electrophiles. *Nat. Chem. Biol.* **8**, 471–476 (2012).
41. Genschik, P., Sumara, I. & Lechner, E. The emerging family of CULLIN3-RING ubiquitin ligases (CRL3s): cellular functions and disease implications. *EMBO J.* **32**, 2307–2320 (2013).
42. Foyn, H. *et al.* Design, synthesis, and kinetic characterization of protein N-terminal acetyltransferase inhibitors. *ACS Chem. Biol.* **8**, 1121–1127 (2013).
43. Shemorry, A., Hwang, C.S. & Varshavsky, A. Control of protein quality and stoichiometries by N-terminal acetylation and the N-end rule pathway. *Mol. Cell* **50**, 540–551 (2013).
44. Polevoda, B., Cardillo, T.S., Doyle, T.C., Bedi, G.S. & Sherman, F. Nat3p and Mdm20p are required for function of yeast NatB N-terminal acetyltransferase and of actin and tropomyosin. *J. Biol. Chem.* **278**, 30686–30697 (2003).
45. Bloes, D.A., Kretschmer, D. & Peschel, A. Enemy attraction: bacterial agonists for leukocyte chemotaxis receptors. *Nat. Rev. Microbiol.* **13**, 95–104 (2015).
46. Boddey, J.A. & Cowman, A.F. Plasmodium nesting: remaking the erythrocyte from the inside out. *Annu. Rev. Microbiol.* **67**, 243–269 (2013).

Acknowledgments

B.A.S., ALSAC, HHMI, and NIH R37GM069530, P30CA021765; J.T.H., NIH F32GM113310; J.W.H., NIH AG011085; J.A.P., NIH DK098285; J.P., NIH GM114260; SJCRH Proteomics Facility, NIH P30CA021765; American Lebanese Syrian Associated Charities. We acknowledge the High Throughput Biosciences Center, Medicinal Chemistry Center, Compound Management, and High Throughput Analytical Chemistry Centers in Chemical Biology and Therapeutics; Hartwell Center for use of their personnel and facilities. We thank J. Lee (Harvard Medical School) for assistance with TMT statistics, E.R. Watson (St. Jude Children's Research Hospital) for purified hNatC enzyme, J. Earl (St. Jude Children's Research Hospital) for photography, R.armorstein (Perelman School of Medicine, University of Pennsylvania) and T. Arnesen (University of Bergen) for NAT constructs, and staff at the BL8.2.1 and 22-ID beamlines at the Advanced Light Source and Advanced Photon Source.

Author contributions

D.C.S., J.T.H., B.S., J.W.H., B.A.S., and R.K.G. designed the research project and analyzed data; D.C.S., J.K.M., S.C.C., A.N.G., and J.M. contributed to assay development; D.C.S., V.O.S., and J.K.M. performed X-ray crystallography; J.T.H., D.B., and H.S.K. designed and performed compound optimization and syntheses; A.A.S. and T.C. contributed to the HTS campaign; D.C.S. performed *in vitro* neddylation experiments and western blotting; M.C. and D.Y.R. generated cell lines; S.-S.O. and M.C. generated the DCN1 shRNA line; I.R.K. and A.F.A. generated DCN1 Flp-In cell lines; Y.C. performed *in vitro* ADME-tox studies to aid in compound optimization; M.C., G.H., and J.L. performed cell-based experiments; D.Y.R., J.A.P., and J.R.C. performed cell-based AP-MS experiments; V.P., X.W., and J.P. performed TMT analysis on proteome samples; all authors contributed to specific parts of the manuscript, and D.C.S., J.T.H., B.A.S. and R.K.G. assume responsibility for the manuscript in its entirety.

Competing financial interests

The authors declare competing financial interests: details accompany the online version of the paper.

Additional information

Any supplementary information, chemical compound information and source data are available in the online version of the paper. Reprints and permissions information is available online at <http://www.nature.com/reprints/index.html>. Publisher's note: Springer Nature remains neutral with regard to jurisdictional claims in published maps and institutional affiliations. Correspondence and requests for materials should be addressed to B.A.S. or R.K.G.

ONLINE METHODS

Constructs, protein preparation, and antibodies. Expression constructs were prepared through standard molecular biology techniques, with coding sequences entirely verified. Mutant versions were generated with a QuikChange kit (Stratagene). DCN proteins used for *in vitro* assays correspond to the isolated PONY domain. For biotinylation of DCN1, an AviTag sequence (GSMISGLNDIFEAQKIEWHEGS) and flanking Gly-Ser linkers between the TEV-cleavage site and the DCN1 PONY domain (DCN1^{PONY}) open reading frame were inserted into a pGEX-based GST-TEV-DCN1 vector. Fusion between a mutant T4 lysozyme (C54T C97A A146T) and DCN1 was generated by overlap PCR and cloned as a histidine-tobacco etch virus (His-TEV fusion in a pRSF-DUET-based vector. Where indicated, two additional mutations (D127A R154A) were further incorporated into lysozyme to prevent inadvertent crystal-packing contacts observed in initial crystals between some inhibitors and a lysozyme symmetry mate. For expression of the trimeric human NatC complex, Naa38 was cloned as a His-TEV fusion into pFastbac-HTB, and Naa30 and Naa35 were cloned untagged into pFastbac1. hNaa10 was cloned as an N-terminal His-maltose-binding protein-TEV fusion in a pRSFDUET-based vector. hNaa50 was cloned with an N-terminal glutathione S-transferase (GST)-TEV tag in a pGEX4T1-based vector. Vectors for expression and purification of hNaa60 and the *S. pombe* NatA complex were kind gifts from R. Marmorstein^{31,32}.

The heterodimeric NEDD8 E1 complex (NAE1-UBA3), NEDD8, CUL1 WHB domain (CUL1^{WHB}), PONY domains of DCN1, DCN2, DCN3, DCN4, DCN5, yNatC, hNaa10, hNaa50, hNaa60, *S. pombe* NatA, and CUL2 (C-terminal domain)-RBX1 were expressed in *Escherichia coli* and purified as previously described^{10,19,31,32,42}. N-terminally acetylated UBE2M and full-length CUL3-RBX1 were expressed in insect cells as previously described^{10,47}. Avi-Tag DCN1 was expressed as a GST-TEV fusion and purified as previously described for GST-TEV-DCN1 (ref. 10). Lysozyme-DCN1 fusions were expressed with an N-terminal His-TEV tag in *E. coli* and purified by nickel-affinity chromatography. Eluted protein fractions from the nickel column were further purified by ion-exchange and gel-filtration chromatography into 25 mM HEPES, 200 mM NaCl, and 1 mM DTT, pH 7.5. The heterotrimeric human NatC complex was expressed in insect cells and purified by nickel-affinity chromatography, liberated by TEV cleavage on beads, and further purified by HiTrap Q ion-exchange and gel-filtration chromatography.

Antibodies to the following proteins were used in this study: CUL1 (sc-17775), actin (sc-1615), CDT1 (sc-365305), DCN1 (sc-81835), DCN1/2 (sc-398218), and p21 (sc-397) from Santa Cruz Biotechnology; CUL3 (A301-109A), Cul4A (A300-739A), and CCNE1 (A301-566A) from Bethyl Laboratories; CUL2 (ab166917), CUL5 (ab184177), and NFE2L2 (ab62352) from Abcam; p27 (610242) from BD Transduction Laboratories; DCN1 (clone 3D7) from Sigma. All commercial antibodies were used according to the manufacturers' instructions, and validation information is available on the manufacturers' websites. Antibodies against UBE2M and DCN1 have been previously described^{24,48}.

Sample sizes. The number of replicates used in each study represents the minimum number of samples required to obtain statistically reliable results, on the basis of our historical experience and power analysis. Briefly, the included experiments were largely exploratory and were designed for the determination of gross changes in response (more than five-fold) at a power of 95% and a *P* value of 5%, taking into account the s.d. observed in similar studies conducted in the laboratories of both R.K.G. and B.A.S. (over 100 similar experiments over 15 years).

Preparation of biotinylated DCN1 and AcUBE2M₁₋₁₂-Alexa Fluor 488 for TR-FRET. Reaction conditions for biotinylation of DCN1 were initially established in small-scale pilot experiments, and the efficiency of Avi-DCN1 biotinylation was assessed on the basis of supershift of biotin-DCN1 in SDS-PAGE after the addition of a stoichiometric excess of avidin (Sigma-Aldrich A9275). Biotinylation reactions contained 90 μM Avi-DCN1 and 4 μM BIRA in 10 mM Tris, 10 mM ATP, 10 mM magnesium acetate, and 2 mM biotin, pH 8.0, and were incubated at room temperature for 2 h. Reaction mixtures were diluted four-fold into 25 mM Tris and 1 mM DTT, pH 8.0, and purified over a HiTrap

Q ion-exchange column. Fractions containing biotin-DCN1 were pooled, concentrated, and further purified by size-exclusion chromatography in 25 mM HEPES, 200 mM NaCl, and 1 mM DTT, pH 7.5.

The hydrocarbon-stapled acetyl-UBE2M₁₋₁₂ peptide corresponding to N-terminally acetylated residues 1–12 of human UBE2M with an additional C-terminal cysteine residue (sequence acetyl-MIKLZ*SLKZ*QKKC, where Z* is 2,4'-pentenylalanine closed after synthesis to create the hydrocarbon staple), was synthesized and purified as previously described¹⁰. For labeling with Alexa Fluor 488 C5 maleimide (Invitrogen A10254), acetyl-UBE2M peptide (7 mg) was dissolved in 5 mL of reaction buffer (50 mM HEPES, pH 7.5, 200 mM NaCl, and 10 mM TCEP) and was then incubated 15 min on ice to allow TCEP to completely reduce the C-terminally appended cysteine residue. The peptide was added dropwise to 0.25 mL of a 26 mM solution of Alexa Fluor dye in DMSO. The mixture was incubated at room temperature overnight, and cold acetone was added (~25 mL) until the solution became turbid. The mixture was spun at 4,000 r.p.m. for 3 min to remove unreacted dye. The precipitated orange residue was dissolved in water and purified by preparative HPLC (Waters 4000, in water/acetonitrile, 0.1% formic acid, with a 5–50% acetonitrile gradient and a flow rate of 15 mL/min, in a 27-min run on a Gemini-NX 5-μm C18 110-Å 50 mm × 30 mm column (Phenomenex). The purified sample was lyophilized, thus yielding ~5 mg of yellow powder with ~90% purity.

TR-FRET assay. TR-FRET assays were carried out in black 384-well microtiter plates at a final volume of 20 μL per well. To screen library compounds, the assay cocktail was prepared as a mixture of 50 nM biotin-DCN1, 20 nM AcUBE2M12-Alexa Fluor 488, and 2.5 nM Tb-streptavidin (Thermo Fisher) in assay buffer (25 mM HEPES, 100 mM NaCl, 0.1% Triton X-100, and 0.5 mM DTT, pH 7.5). The assay cocktail was incubated for 1 h at room temperature and distributed with a WellMate instrument (Matrix). Compounds to be screened were added to assay plates from DMSO stock solutions by pin transfer with 50SS pins (V&P Scientific). The assay mixture was incubated for 1 h at room temperature before measurement of the TR-FRET signal with a PHERAstar FS plate reader (BMG Labtech) equipped with modules for excitation at 337 nm and emission at 490 and 520 nm. The integration start was set to 100 μs, and the integration time was set to 200 μs. The number of flashes was fixed at 100. The 520/490 ratio was used as the TR-FRET signal in calculations. Assay endpoints were normalized from 0% (DMSO only) to 100% inhibition (unlabeled competitor peptide) for hit selection and curve fitting. Data curves in **Figure 2c** and **Supplementary Figures 1c, 2b** and **8b,c** are fits to an average of *n* = 3 independent experiments.

HTS campaign. Initial screening was performed at a single point concentration of 30 μM with a library of approximately 600,000 compounds. The HTS endeavor was implemented on a fully automated system (HighRes Biosolutions) with an integrated robotic arm (Stäubli). The protein and peptide master mixture were kept chilled at 4 °C and were dispensed into solid black 384-well assay plates (20 μL/well) with Matrix Wellmate bulk dispensers (Thermo Fisher), and plates were then centrifuged with a V-Spin plate centrifuge (Agilent Technologies). Test articles and controls (stored as 10 mM solutions in DMSO donor plates) were transferred to the assay plates with a pin tool (V&P Scientific) equipped with FP1S50 pins, thus resulting in final compound concentrations of 30 μM. The TR-FRET signal was acquired after the plates were incubated for 1 h at room temperature in dedicated incubators (Liconic Instruments). Dose-response curve fitting and chemical-structure network graph analysis were performed as previously described⁴⁹. Compound solubility, permeability, and inhibition of proliferation were performed as previously described⁵⁰.

Enzyme assays in pulse-chase format monitoring DCN1-dependent cullin neddylation. Enzymatic neddylation of cullins was monitored with pulse-chase assays isolating the reaction stimulated by DCN1 from upstream reactions in the E1-E2-E3 NEDD8 transfer cascade^{10,20}. NEDD8 was labeled with fluorescein-5-maleimide on an N-terminal cysteine-containing tag, as previously described²⁰, and was thioester-linked to N-terminally acetylated UBE2M in a pulse reaction with 10 μM UBE2M, 15 μM labeled NEDD8, and 400 nM APPBP1-UBA3 in 25 mM HEPES, 200 mM NaCl, 2.5 mM MgCl₂, and 1 mM

ATP, pH 7.5 for 15 min at room temperature. After this reaction was quenched for 5 min on ice with 50 mM EDTA, NEDD8 was chased from AcUBE2M to a cullin, either CUL2 C-terminal domain in complex with RBX1 or full-length CUL3 in complex with RBX1. Our default assays generally used CUL2 as the neddylation substrate because (i) cullin proteins are generally expressed at low levels, but our yields for recombinant CUL2 were ~20 fold better, thus making it most practical to perform experiments with CUL2; (ii) DCN1 has a higher affinity for CUL2 (K_d ~500 nM)¹⁹, thus allowing for a higher percentage saturation of CUL2 with DCN1 under the low protein concentration conditions of our chase assay. This aspect was important for sensitizing the assays to allow for detection of DCN1-dependent neddylation rather than reactions in the absence of DCN1, without having to use very high concentrations of DCN1. Chase reactions were performed by diluting the thioester-linked UBE2M~NEDD8 conjugate to 0.04 μ M in 50 mM Tris, 50 mM NaCl, 50 mM EDTA, and 0.5 mg/mL BSA, pH 6.8, on ice. Reactions were initiated by the addition of CUL~RBX complex alone or in a 1:1 mixture with the indicated DCN family member to a final concentration of 125 nM. Aliquots were removed at the indicated times and terminated with 2 \times SDS~PAGE sample buffer. Reaction products were separated on 4–12% NuPAGE gels (Invitrogen). Fluorescent gels were visualized by scanning on a Typhoon imager (GE).

Assaying N-terminal acetyltransferase activity. Synthetic peptide substrates NH₂-MIKLFSLKQKKEESAGGKTKGSSKK, NH₂-EEEEIALRWGRPVGRRRPVRVYP, NH₂-SESSKSRWGRPVGRRRRPVRVYP, NH₂-MLGPEGGRWRPVGRRRRPVRVYP, and NH₂-MAPLDDRWRPVGRRRRPVRVYP were synthesized and HPLC purified to >98% purity by the Hartwell Center at St. Jude. N-terminal acetylation of peptide substrates was monitored with an assay using 5,5'-dithiobis-(2-nitrobenzoic acid) (DTNB)⁴². Purified Nat enzyme (100 nM *S. pombe* NatA, 200 nM γ NatC, hNatC, hNaa10, hNaa50, or hNaa60) was mixed with 500 μ M substrate peptide and 500 μ M acetyl-CoA (Sigma) in acetylation buffer (25 mM HEPES, pH 7.5, 100 mM NaCl, and 1 mM EDTA) in a final reaction volume of 50 μ L. Reactions for γ NatC, hNatC, *S. pombe* NatA, and hNaa10 were carried out at room temperature, whereas assays with hNaa50 and hNaa60 were at 37 $^{\circ}$ C. At the indicated times, the reactions were quenched by the addition of 100 μ L 3.2 M guanidinium HCl, 100 mM sodium phosphate dibasic, and 10 mM EDTA, pH 6.8. 20 μ L of a freshly made 10 mg/mL DTNB solution in 100 mM sodium phosphate dibasic, 10 mM EDTA, pH 6.8 was added to the quenched samples and incubated for 5 min at room temperature. Samples were further diluted to a final volume of 510 μ L with 2.13 M guanidinium HCl, 66.6 mM sodium phosphate dibasic, and 6.66 mM EDTA, pH 6.8. The absorbance of the samples at 412 nm was recorded, and the amount of product formed was calculated by using the extinction coefficient of 13,700 M⁻¹ cm⁻¹.

Crystallography. Crystals were grown by the hanging-drop vapor-diffusion method. For lysozyme~DCN1~compound complex structures, mixtures were prepared by dilution of lysozyme~DCN1 to 50 μ M in 50 mM HEPES and 150 mM NaCl, pH 7.5. Compounds were subsequently added to a final concentration of 75 μ M from concentrated DMSO stock solutions (1–2% DMSO final concentration) and incubated on ice for 1 h to equilibrate binding. The mixture was then concentrated approximately 10- to 12-fold with an AmiconUltra concentrator before crystal screens. For the DCN4~CUL1^{WHB} complex structure, the purified proteins were mixed in stoichiometric levels, incubated on ice for 1 h, and concentrated to a final complex concentration of approximately 700 μ M.

For lysozyme~DCN1~NAcM complex structures, we first crystallized apo-lysozyme~DCN1 at 4 $^{\circ}$ C in 11–13% PEG 3350, and 0.2 M NH₄Br, thus resulting in large clumped crystals. Clusters of apo crystals were crushed and used as seed stocks for generating diffraction-quality lysozyme~DCN1~NAcM crystals by streak seeding into 6–9% PEG 3350 and 0.2 M NH₄Br. Crystals were harvested in mother liquor supplemented with 25% MPD before being flash frozen in liquid nitrogen. Reflection data were collected at beamline 8.2.1 at the Advanced Light Source. The crystals belonged to space group *P*₂, and had one lysozyme~DCN1~inhibitor complex in the asymmetric unit. Phases for all structures were obtained by molecular replacement with PHASER⁵¹ with the following search models: one copy each of (i) residues 6–158 from a prior structure of lysozyme (PDB 2LZM) and (ii) residues 65–250 from a prior structure

of DCN1 (PDB 3TDU). After initial rounds of building and refinement, small molecules were fit into the density with COOT⁵² by using compound restraint files generated with the PRODRG server⁵³. In all cases, manual building was performed with COOT, and refinement was performed with Phenix⁵⁴. Additional details of the refinement are provided in **Supplementary Table 2**. The final Ramachandran statistics are as follows: lysozyme~DCN1~NAcM-HIT, 99% favored, 0% outliers; lysozyme~DCN1~NAcM-OPT, 99% favored, 0% outliers; lysozyme~DCN1~NAcM-COV, 98% favored, 0% outliers.

Crystals of DCN4^{PONY}~CUL1^{WHB} grew at 4 $^{\circ}$ C in 25% PEG 3350, 0.2 M LiSO₄, 10 mM TCEP, and 0.1 M BTP, pH 6.5 as sea-urchin-like needle clusters. Single diffraction-quality crystals were obtained by streak seeding into 19% PEG 3350, 0.2 M LiSO₄, 10 mM TCEP, and 0.1 M BTP, pH 6.3. Crystals were harvested from mother liquor and soaked in step gradients for 5 min, with sequential soaks in well solution supplemented with 12% and 24% glycerol before flash freezing in liquid nitrogen. Reflection data were collected at the SERCAT 22-ID beamline at the Advanced Photon Source. The crystal belonged to space group *C*₂ with one copy of the DCN4~CUL1 complex in the asymmetric unit. Phases were obtained by molecular replacement with PHASER⁵¹, with the following search models: one copy each of (i) residues 65–250 from a prior structure of DCN1 (PDB 3TDU) and (ii) residues 705–770 from a prior structure of CUL1 (PDB 3TDI). The electron density surrounding the CUL1^{WHB} was weak, presumably because of a lack of participation in crystal packing. Therefore we modeled and built this chain largely from a prior high-resolution and high-quality structure of CUL1^{WHB}, PDB 3TDU. Manual rebuilding was performed with COOT, and refinement was performed with Phenix^{52,54}. Additional details of the refinement are provided in **Supplementary Table 2**. The final Ramachandran statistics were as follows: CUL1^{WHB}~DCN4, 99% favored, 0% outliers.

Bromodomain profiling. Compound profiling against a panel of 32 BRDs was performed by DiscoverRX Corp. at a single concentration of 10 μ M. The amount of BRD captured on an immobilized ligand in the presence or absence of compound was measured with a qPCR method detecting the associated DNA label tagged to the BRD. Any targets that demonstrated \geq 40% inhibition at 10 μ M were subjected to dose~response profiling for K_d determination. An 11-point three-fold serial dilution of each test compound was prepared in 100% DMSO at 1,000 \times final test concentration (top concentration 120 μ M), such that the final concentration of DMSO was 0.09% in the assay (**Supplementary Data Set 4**).

Histone deacetylase, sirtuin, and histone acetyltransferase profiling. Compound profiling against a panel of 11 histone deacetylases, 4 sirtuins, and 7 histone acetyltransferases was performed by Reaction Biology Corp. at a single concentration of 10 μ M in triplicate. The results are reported as percentage enzyme activity compared with that of DMSO-treated controls (**Supplementary Data Sets 3 and 5**).

Cell culture. HCC95, a squamous cell lung carcinoma line; BJ, a normal human foreskin fibroblast cell line; HEK293T, an embryonic kidney line; and HCT116, a human colon cancer cell line were purchased from the American Type Culture Collection (ATCC). CAL-33, a tongue squamous cell carcinoma line, was purchased from the Leibniz Institute DSMZ-German Collection of Microorganisms and Cell Cultures. BJ cells were cultured as recommended. HCT116 cells were cultured in McCoy's 5a medium with 10% FBS and 2 mM L-glutamine. HCC95 cells were cultured in RPMI-1640 medium supplemented with 10% FBS and 2 mM L-glutamine. HEK293T and CAL-33 cells were cultured in DMEM (Thermo Fisher) supplemented with 10% FBS (Hyclone). Cell culture media were purchased from ATCC, and FBS was purchased from GE Healthcare Hyclone. Cells were routinely tested for mycoplasma contamination with a MycoAlert Mycoplasma Detection Kit (Lonza).

Stably transfected human embryonic kidney (HEK) 293 Flp-In T-Rex cells (Thermo Fisher) were cultured in DMEM supplemented with 10% FBS, 2 mM L-glutamine, and antibiotics (100 units/mL penicillin and 0.1 mg/mL streptomycin), and in the presence of selection with 100 μ g/mL hygromycin and 15 μ g/mL blasticidin. HA-tagged DCN1 expression vectors (pcDNA5-FRT/TO+HA-DCN1 or pcDNA5-FRT/TO+HA-DCN1(D211A A235R

D241)) were stably transfected into HEK293 T-Rex with Invitrogen's Flp-In T-Rex system, according to the manufacturer's instructions. Protein expression was induced for the times indicated with 1 $\mu\text{g}/\text{mL}$ doxycycline.

Sequence validated, C-terminally FLAG-HA tagged UBE2M³⁴ was transfected with TransIT-293 transfection reagent (Mirus Bio) in combination with viral helper constructs (VSVG, TAT1B, MGPM2, and CMV-Rev1B). Viral particles were harvested, and a stable cell line was created by infection of HEK293T cells and subsequent selection with puromycin (Life Technologies).

SMARTvector lentiviral shRNA was obtained from Dharmacon (source clone ID V3SVHS00_5390398; microRNA sequence TAGTCTGCGCTTACCTTAC). Lentivirus particles were transduced into HCC95, and a stable clone was selected according to the manufacturer's recommendations.

Soft-agar colony-formation assays were conducted according to previously described protocols⁵⁵. Colonies were visualized with a nitroblue tetrazolium chloride solution and imaged with a Nikon DSLR camera and light box. Colonies were defined as groupings of more than 20 cells and were counted manually. Shown are representative well images from individual experiments that were individually repeated at least three times.

Western blot analysis. Exponentially growing cells were plated in six-well plates at 0.4×10^6 cells/well in 2 mL of medium and incubated overnight at 37 °C in a humidified 5% CO₂ incubator. 24 and 48 h after plating, the medium was aspirated and replenished with 2 mL fresh medium containing either 4 μL of DMSO or a 500 \times compound DMSO stock solution. The cells were harvested after 72 h via trypsinization, thoroughly washed with PBS, pelleted, flash frozen in liquid N₂, and stored at -80 °C. Cell pellets were thawed on ice and lysed by harvested resuspension in 30–40 μL of lysis buffer (50 mM Tris, 150 mM NaCl, 0.5% NP-40, 0.1% SDS, 6.5 M urea, 2 mM 1,10-orthophenanthroline, 1 \times Halt protease- and phosphatase-inhibitor cocktail (Thermo Fisher), and 0.25 kU Universal Nuclease (Thermo Fisher), pH 7.5). Cell suspensions were incubated on ice for 25 min with occasional mixing by pipetting up and down. Lysates were cleared by centrifugation at 13,000 r.p.m. for 20 min, and the supernatant was collected. The protein concentration of total cell lysate was determined with BCA assays (Pierce) by using BSA as a control. Cell lysates were diluted into 2 \times SDS-PAGE sample buffer, such that 25 μg of total protein was loaded per well. Samples were heated at 95 °C for 2 min, briefly cleared by pulse centrifugation, separated on 4–12% NuPAGE gels (Invitrogen), and transferred to PVDF membranes (Bio-Rad) at 100 V for 90 min at 4 °C. Membranes were blocked for 1 h in blocking buffer consisting of 1 \times Tris-buffered saline, 0.1% Tween-20, and 5% blotting-grade nonfat dry milk (Bio-Rad). Primary antibodies were prepared in blocking buffer and incubated with membranes overnight at 4 °C with rocking, and membranes were then extensively washed in 1 \times Tris-buffered saline and 0.1% Tween-20. Secondary antibodies were prepared in blocking buffer according to the manufacturer's recommendations and incubated with membranes for 1 h at room temperature. After being extensively washed, membranes were developed with SuperSignal West Pico chemiluminescent substrate (Thermo Fisher) and developed by film exposure (HyBlot CL, Denville Scientific). Shown are representative results from one experiment that was repeated independently three times.

Whole-proteome profiling by tandem mass tagging (TMT) and mass spectrometry. The experiment was performed with a previously published protocol with slight modifications^{56,57}. Briefly, proteins were extracted from cell pellets and digested with LysC (Wako) and trypsin (Promega). The resulting peptides were desalted with C18 cartridges (Harvard Apparatus) and chemically labeled with decaplex TMT reagents (Thermo Fisher). The labeled samples were mixed equally, desalted, and fractionated through offline basic pH reversed-phase liquid chromatography (RPLC, pH 8.0, XBridge C18 column, 4.6 mm \times 25 cm, 3.5- μm particle size, Waters). The fractions were then analyzed by acidic-pH RPLC-MS/MS analysis (75 μm \times ~40 cm, 1.9- μm C18 resin from Dr. Maisch, Q-Exactive HF from Thermo Fisher).

Peptide and protein identification from MS/MS raw data was carried out with JUMP, a newly developed tag-based hybrid search engine that combines pattern matching and *de novo* sequencing to score putative peptides for high sensitivity⁵⁸. The data were searched against the UniProt human database

concatenated with a reversed decoy database to evaluate the false discovery rate (FDR) and were then filtered on the basis of mass accuracy and matching scores to decrease the FDR to ~1%. The quantitative analysis was processed by the JUMP software suite as previously described⁵⁶ (**Supplementary Data Set 8**).

TMT interaction proteomics data analysis. Mass spectra were processed with a Sequest-based in-house software pipeline⁵⁹. Searches were performed against all entries from the human UniProt database (11 March 2014) including all protein sequences in reverse order. The precursor tolerance was set to 50 p.p.m., and the product-ion tolerance was set to 1.0 Da. TMT tags on lysines and N termini (+229.163 Da) and carbamidomethylation of cysteine residues (+57.021 Da) were set as static modifications, and oxidation of methionine residues (+15.995 Da) was set as a variable modification. Peptide-spectrum matches (PSMs) were adjusted to a 2% FDR through linear discriminant analysis⁵⁹. For each peptide, a total minimum signal-to-noise value of 100 was required⁶⁰. Changes in protein abundance were determined from reporter-ion intensities averaged across all peptides for a given protein. Data analyses for TMT-immunoprecipitation were carried out with the R statistical package (version 3.2.3). TMT channel intensities were normalized to the bait-peptide intensity and then quantile normalized. The data were log transformed, and FDR-adjusted *P* values were determined through an empirical Bayes approach. Differential interactors were determined on the basis of a fold-change threshold of 1.5 and an FDR threshold of 0.05 (**Supplementary Data Set 6**).

IP-MS to examine N-terminal acetylation of UBE2M. Cells expressing UBE2M FLAG-HA were treated for 24 h with 10 μM of NAcM-COV dissolved in DMSO or with DMSO alone. Cells were lysed in 50 mM Tris, pH 7.5, 150 mM NaCl, and 0.5% NP-40 with protease inhibitors (Roche) to generate whole cell lysates. Clarified lysates were immunoprecipitated with anti-FLAG magnetic beads (Sigma). Complexes were washed four times with lysis buffer and twice with PBS, then eluted with FLAG peptide at room temperature. Eluted proteins were reduced with DTT and alkylated with iodoacetamide, then TCA precipitated. TCA-precipitated proteins were digested with Glu-C (Thermo Fisher), then cleaned up with C-18 stage tips. Eluted peptides were resuspended in 5% formic acid and 5% acetonitrile. Data were collected with a Q Exactive mass spectrometer (Thermo Fisher) coupled with a Famos autosampler (LC Packings) and an Accela600 liquid chromatography (LC) pump (Thermo Fisher). Peptides were separated on an ~18-cm column with 100 μm inner diameter. For each analysis, we loaded ~1 μg onto the column. Peptides were separated with a 70-min gradient of 5–29% acetonitrile in 0.125% formic acid with a flow rate of ~300 nL/min. For the MS1 scan, resolution was set to 70,000 with an automatic gain control (AGC) target 1×10^5 and a maximum injection time of 250 ms. We selected the top 20 precursors for HCD MS2 analysis with the following parameters: resolution, 17,500; AGC 1×10^5 ; maximum injection time, 60 ms; isolation window, 2 Th; normalized collision energy (NCE), 25; and centroid spectrum data type. In addition, unassigned and singly charged species were excluded from MS2 analysis, and dynamic exclusion was set to automatic.

Data availability. Structural data have been deposited in the Protein Data Bank under accession numbers PDB 5V83 (DCN1–NAcM-HIT), PDB 5V86 (DCN1–NAcM-OPT), PDB 5V88 (DCN1–NAcM-COV), and PDB 5V89 (DCN4^{PONY}-CUL1^{WHB}). All other data generated or analyzed during this study are included in this published article (and its supplementary information files) or are available from the corresponding author on reasonable request.

- Scott, D.C. *et al.* Two distinct types of E3 ligases work in unison to regulate substrate ubiquitylation. *Cell* **166**, 1198–1214.e24 (2016).
- Huang, D.T. *et al.* A unique E1-E2 interaction required for optimal conjugation of the ubiquitin-like protein NEDD8. *Nat. Struct. Mol. Biol.* **11**, 927–935 (2004).
- Guiguemde, W.A. *et al.* Chemical genetics of *Plasmodium falciparum*. *Nature* **465**, 311–315 (2010).

50. Min, J. *et al.* Optimization of a novel series of ataxia-telangiectasia mutated kinase inhibitors as potential radiosensitizing agents. *J. Med. Chem.* **59**, 559–577 (2016).
51. McCoy, A.J. *et al.* Phaser crystallographic software. *J. Appl. Crystallogr.* **40**, 658–674 (2007).
52. Emsley, P. & Cowtan, K. Coot: model-building tools for molecular graphics. *Acta Crystallogr. D Biol. Crystallogr.* **60**, 2126–2132 (2004).
53. Schüttelkopf, A.W. & van Aalten, D.M. PRODRG: a tool for high-throughput crystallography of protein-ligand complexes. *Acta Crystallogr. D Biol. Crystallogr.* **60**, 1355–1363 (2004).
54. Adams, P.D. *et al.* PHENIX: a comprehensive Python-based system for macromolecular structure solution. *Acta Crystallogr. D Biol. Crystallogr.* **66**, 213–221 (2010).
55. Borowicz, S. *et al.* The soft agar colony formation assay. *J. Vis. Exp.* **92**, e51998 (2014).
56. Niu, M. *et al.* Extensive peptide fractionation and γ 1 ion-based interference detection method for enabling accurate quantification by isobaric labeling and mass spectrometry. *Anal. Chem.* **89**, 2956–2963 (2017).
57. Bai, B. *et al.* Deep profiling of proteome and phosphoproteome by isobaric labeling, extensive liquid chromatography, and mass spectrometry. *Methods Enzymol.* **585**, 377–395 (2017).
58. Wang, X. *et al.* JUMP: a tag-based database search tool for peptide identification with high sensitivity and accuracy. *Mol. Cell. Proteomics* **13**, 3663–3673 (2014).
59. Huttlin, E.L. *et al.* A tissue-specific atlas of mouse protein phosphorylation and expression. *Cell* **143**, 1174–1189 (2010).
60. Paulo, J.A., O'Connell, J.D. & Gygi, S.P. A triple knockout (TKO) proteomics standard for diagnosing ion interference in isobaric labeling experiments. *J. Am. Soc. Mass Spectrom.* **27**, 1620–1625 (2016).